Green-Engineered Ni–Cd Ferrite Nanostructures For Superior Photocatalytic Activity

Rohini Patil

Department of Physics, Sanjivan Engineering and Technology,Panhala, Kolhapur M. S. India

Abstract

The aim of the existing study is to biofabricated of cadmium substituted nickel ferrite and corresponding reusable catalytic behavior. Among all of this substitution the $Ni_{0.2}Cd_{0.8}Fe_2O_4$ NRs as an effective catalyst through a straightforward and environmentally friendly biosynthesis way utilizing cabbage leaf extract. we are the first to investigate the photocatalytic efficacy of various substitution of cadmium in nickel ferrites synthesized with cabbage leaf extract for the photodegradation of methylene orange under UV-Vis light. Additionally, we examined the influence of hydrogen peroxide, the amount of photocatalyst used, and recyclability, among other factors, to determine the optimal conditions for the photodegradation of MO.

$Ni_{0.2}Cd_{0.8}Fe_2O_4$ NRs confirmed the formation of single-phase cubic spinel structure with 28.35nm crystallite size and SEM observation indicates a rod shape nanoparticle which is good agreement with TEM analysis. The optimized $Ni_{0.2}Cd_{0.8}Fe_2O_4$ magnetic NRs having degradation of MO efficiency reached 99 % under UV light irradiation at 45 min whereas other substitution of cadmium such as x= 0.2,0.4,0.6 corresponding degradation efficiency is 64, 74, 80, 88 % respectively. Also, we studied the addition of H_2O_2 the degradation efficiency could be increased from 80 to 99% within 45 min under UV-Vis. light.

Key words : Photocatalyst, Ni-Cd Ferrite, Nanorods, Methyl Orange, 99 % degradation

Introduction

The modernization and advancement of diverse industries, coupled with the unrestrained application of agricultural chemicals, have culminated in the accumulation of substantial quantities of highly deleterious pollutants in the environment [1-2]. These pollutants inflict harm upon the ecosystem and serve as primary contributors to infectious diseases, thereby impacting human health and natural systems. Consequently, environmental pollution has escalated into a pressing global issue, and the efficient eradication of these pollutants is critically imperative for environmental sustainability. A range of methodologies has been devised for the remediation of pollutants [3-4]. Among these approaches, photocatalysis has emerged as a particularly promising technique.

Ferrites are renowned for their widespread applications in the domain of electro-magnetic NMs [5]. However, here are relatively rare studies concerning their photocatalytic applications. Ferrites present a notable advantage by offering optimal light can be articulated as the most effective capture of light for photons with minimal energy and possessing a highly suitable electronic, magnetic morphological structure for photocatalytic purposes [6].

In the context of photocatalysis, ferrites demonstrate significant utility. Numerous endeavours have been undertaken to synthesize narrow band gap ferrite semiconductors capable of harnessing a broader portion of the visible spectrum. Recent studies served as a significant indicator of potential for visible light active photocatalytic applications of spinel ferrites [7].

Nickel ferrites have been the focus of extensive research due to their photo stability, cost-effectiveness, ease of synthesis, and broad range of applications. Furthermore, the optical properties of nickel ferrite nanoparticles, particularly their band gap value of approximately 2.1 eV, indicate a good light absorption capacity within the visible spectrum, capable of generating reactive oxygen species ($\bullet O_2$) under light irradiation [8]. Additionally, separation of nanoparticles has demonstrated considerable reusability in the degradation of dye pollutants [9].

Cadmium ferrite is another class of ferrites, have garnered significant attention due to their strong light absorption capacity, efficient charge transport, chemical stability, and narrow band gap of 1.97 eV [10]. Consequently, cadmium ferrite NPs are promising candidate for the removal and degradation of pollutants from wastewater under solar irradiation [7], exhibiting excellent photocatalytic properties for dye degradation.

Extensive research has been conducted on the synthesis of nickel -cadmium materials. Kafeshani et al. reported on Ni-Cd co-doped $SrTiO_3$ photocatalysts achieving notable degradation of methylene blue within 60 minutes of irradiation. [11] Khan et al. reported that the incorporation of Cd and Ni could substantially enhance photocatalytic activity. [12] Likewise, Kebede et al. demonstrated that increasing the concentration of coupled Ni-Cd in $BiFeO_3$ markedly improved photocatalytic performance [13].

In recent times, ferrite nanocatalysis has come to the forefront and widely utilized "green" technology for the remediation of contaminated water. This approach is particularly significant in the context of photocatalysis research, which is based crucial focus within on the method of preparation. Extensive techniques exist for synthesizing Ni-Cd, including coprecipitation, auto combustion, and sintering methods. [14-16]. However, we employed a green synthesis method, a straightforward and economical approach using plant as a stabilizing agent. This method yields nanosized ferrites with a high degree of crystallinity, uniform particle sizes, and energy efficient. It also ensures high purity, with no reactions occurring with containers, thereby enhancing the overall purity of the final product [17].

The aim of the existing study is to biofabricated $Ni_{0.2}Cd_{0.8}Fe_2O_4$ NRs as an effective catalyst through a straightforward and environmentally friendly biosynthesis way utilizing cabbage leaf extract. To the best of our understanding, informed by a comprehensive review of the literature, we are the first to investigate the photocatalytic efficacy of $Ni_{0.2}Cd_{0.8}Fe_2O_4$ nanorods synthesized with cabbage leaf extract

for the photodegradation of methylene orange under UV-Vis light. Additionally, we examined the influence of hydrogen peroxide, the amount of photocatalyst used, and recyclability, among other factors, to determine the optimal conditions for the photodegradation of MO.

Experimental Section

Materials

All chemicals employed in this study were of analytical grade and utilized without any additional purification. Methyl Orange, Propanol, Potassium Hydroxide, Nickel Nitrate (99.9% purity), Cadmium Nitrate (99.9% purity) and Iron Nitrate (99.9 % purity) were purchased from Thomas Baker Chemicals (Mumbai, India). Double distilled water (DW) was used as a solvent for the preparation of solutions.

Cabbage Leaf Extraction

To prepare the cabbage (Brassica oleracea L.) leaf extract, fresh organic cabbage leaves were sourced from a reputable vegetable farm located near Kolhapur, India. Initially, cabbage leaves were carefully handpicked from the farm. These leaves were chosen for their organic origin and pristine quality. To eliminate any potential contaminants, the leaves were meticulously washed using a copious amount of distilled water. the cleaned cabbage leaves were transformed into smaller pieces using a kitchen knife. This step was undertaken to facilitate efficient extraction. The juice extraction process involved using a single grinder. Specifically, 25 grams of finely cut cabbage leaf pieces were combined with 250 mL of distilled water within the grinder. This mixture was processed to obtain the cabbage leaf extract. The extracted juice was subjected to gentle boiling for 2 minutes. The boiled extract was cooled at room temperature and filtered through Whatman paper 41 to remove the solid residue. Finally, the obtained extract was used for the fabrication of $NiCdFe_2O_4$ NPs.

Synthesis of $NiCdFe_2O_4$ NPs

In a synthesis of $Ni_{1-x}Cd_xFe_2O_4$ NPs precursors such as nickel nitrate (0.2 M), cadmium nitrate (0.8 M), and iron nitrate (2 M) were each separately dissolved in 100 mL of distilled water, maintaining a 1:2 molar ratio. The solutions of nickel nitrate, cadmium nitrate, and iron nitrate are thoroughly mixed to ensure homogeneity and preheated to 80°C, with the addition of 40 mL of cabbage plant extract as a stabilizing agent. Subsequently, an aqueous KOH solution (1 M) is added dropwise over 4 hours with constant stirring to achieve the desired precipitate. The resulting brown solution indicates the formation of $Ni_{0.2}Cd_{0.8}Fe_2O_4$ NRs the solution is then centrifuged and washed multiple times with water, followed by alcohol, to remove any residual plant matter, and the resulting fine powder is obtained by grinding in a mortar and pestle. Finally, the calcination process was conducted at 700°C to yield $Ni_{0.2}Cd_{0.8}Fe_2O_4$ NRs. This process is repeated for various cadmium concentrations, such as 0.4, 0.6 and 0.8 with corresponding adjustments in composition. diagrammatic depiction of the synthesis of $NiCdFe_2O_4$ NPs is presented in Fig. 1.

Green Synthesis Route of $NiCdFe_2O_4$ NPs

The plausible mechanism of $NiCdFe_2O_4$ NPs is illustrated in Fig.2. The various concentration of salts like Ni $(NO_3)_2.6H_2O$, Cd $(NO_3)_{2.}$ $6H_2O$ and Fe $(NO_3)_{3.}$ $6H_2O$ are mixed with leaf extract and ions of Ni^{2+}, Cd^{2+} and Fe^{3+} are distribute consistently and form a complex with active sites of -OH groups. After annealing the obtained network undergo inactive decomposition. It meant that the polyphenolic molecules interact with Ni^{2+}, Cd^{2+} and Fe^{3+} ions developing connection between -OH groups from two different chains comes from polyphenolic group. The generated cations keep the molecules together and form various structures of Ni^{2+}, Cd^{2+} and Fe^{3+} complex [18].

Characterization of $NiCdFe_2O_4$ NPs

Powder X-ray diffraction patterns of the $Ni_{1-x}Cd_xFe_2O_4$(x=0 to 0.8) NPs were meticulously recorded using a D-8 Advance Diffractometer. (Bruker-AXS, Germany) The instrument was operated at 40 kV, employing CuKα radiation with a wavelength of 1.542 Å. The scanning procedure encompassed the (2θ spanning from 10 to 80 ^{0}with a scanning rate of 2 min per degree). The crystalline phases were identified by comparing the obtained patterns with corresponding JCPDS files. The surface morphology of the sample $Ni_{1-x}Cd_xFe_2O_4$(x=0, 0.2, 0.4, 0.6, 0.8) NPs was estimated by Scanning Electron Microscope (JSM, 6390 JEOL, Japan). This instrument was equipped with an EDS detector to provide elemental analysis. FT-IR spectra were meticulously recorded using an FT-IR-8700 Perkin-Elmer spectrophotometer (Japan). Spectra were obtained with a high resolution of 4 cm^{-1} across the range of 4000-400 cm^{-1}, providing valuable insights into the sample's chemical composition. The UV-Vis DRS of the $Ni_{1-x}Cd_xFe_2O_4$(x=0, 0.2, 0.4, 0.6, 0.8) NPs were acquired using a Spectrometer (UV-2450 Shimadzu, Japan). This technique allows for the assessment of the sample's optical properties. The magnetic property of the sample was scanned by a Vibrating Sample Magnetometer (VSM, 7400-S, Lakeshore, USA) with an applied field sweeping between ±10,000 Oe at room temperature.

Determination of Photocatalytic Activity

The investigation of photocatalytic activities was carried out utilizing eco-friendly $Ni_{1-x}Cd_xFe_2O_4$(x=0, 0.2, 0.4, 0.6, 0.8) NPs for the degradation of Methyl Orange (MO) is an aqueous medium, employing UV-Vis's illumination with a wavelength of 365 nm. The photochemical study was conducted within a photoreactor, with continuous stirring facilitated by a magnetic stirrer, and illumination was provided by a high-pressure mercury lamp (250 W, Philips HPL-N), all at room temperature. A known quantity of cadmium substituted $NiCdFe_2O_4$ photocatalyst introduced into an aqueous MO solution (20 ppm, 100 mL). Continuous stirring was maintained for 30 minutes in complete darkness to reach adsorption-desorption equilibrium subsequently, 3 mL of the suspension was carefully decanted at fixed time intervals. To maintain the temperature of the outer jacket, a continuous flow of water was maintained. The degradation of MO, as evidenced by changes in absorbance, was monitored using a UV-Vis-NIR Spectrophotometer (UV-3600, Shimadzu). Additionally, the influence of various catalyst loadings

(ranging from 1.0 to 2.0 g/dm^3) was systematically investigated through experimental studies. The photocatalytic degradation efficiency (η %) was calculated with equation

Results and Discussion

XRD Analysis

Fig. 3 exhibits XRD patterns of $Ni_{1-x}Cd_xFe_2O_4$ at (x= 0,0.2, 0.4, 0.6 and 0.8) and the content of Cd increases from 0.0 to 0.4 there is existence of Ni peaks, this may be attributed to the low concentration of Cd. Content of Cd rises from 0.6 to 0.8, there is existence of Cd peaks it may due to the low concentration of Ni. and of (220), (311), (222), (400), (422), (511), (440) (620) and (533) corresponding to diffraction peaks at (2θ) values are 29.15, 34.15, 35.68, 41.48, 51.40, 54.79, 60.11, 68.08 and 70.96 (JCPDS data No-65-3115), ($CdFe_2O_4$) Similar behavior reported in these article [19] no.10-0325($NiFe_2O_4$) .The observed peak confirmed the formation of crystalline and single-phase cubic spinel structure of $NiCdFe_2O_4$ NPs without any impurities and to find the as usual crystallite size of synthesized $Ni_{1-x}Cd_xFe_2O_4$ at (x= 0,0.2, 0.4, 0.6 and 0.8) by Debye-Scherrer's equations

From Table 1, it is found that the content of Cd^{2+} increases as the corresponding crystallite size rises from 12.87 nm to 28.35 nm. From XRD It is noted that the (311) peak position shifts progressively towards a lower angle, indicating a steady increase in the lattice parameter from 8.33 Å to 8.50 Å with growing Cd substitution, which is in good agreement with Vegard's law (20). The incorporation of Cd^{+2} ions shifts the Fe^{3+} ions from tetrahedral to octahedral sites, and the higher ionic radius of Cd (0.097 nm) expands the lattice [21]. The density rises due to the higher atomic weight of cadmium compared to that of nickel. [22] similar results are reported in this article [15]. Additionally, the average volume of $Ni_{1-x}Cd_xFe_2O_4$ was calculated, with the highest volume recorded at 614.12 Å^3 at higher content of Cd resulting, volume is high which enhances photocatalytic activity (23). The calculated values for lattice constant, crystallite size, X-ray density and volume are detailed in Table 1.

FT-IR Analysis:

By using FT-IR spectroscopy, we determined both intermolecular interactions and functional groups of the various composite of the $Ni_{1-x}Cd_xFe_2O_4$ NPs at (x= 0.2to 0.8). which is recorded in the range of 3500-500 cm^{-1} are presented in Fig. 4 For x=0.8, the spectra displayed prominent bands at 1030, 1475, 1647, 1759, 2860, 2936, and 3438 cm^{-1} Notably, the peak at around (601 cm^{-1}) is attributed to the vibrational stretching at the tetrahedral (M-O bond), while the peak at approximately 430 cm^{-1} corresponds to the octahedral metal-oxygen bond [24,25]. These two bands signify the characteristic features of the MFe_2O_4 spinel structure, confirming the formation of $NiCdFe_2O_4$ NPs as spinel structures [26,27]. Furthermore, the peak at 1038 cm^{-1} can be assigned to O-H bending vibration, while the range from 2345-2365 cm^{-1} is ascribed to H-O-H bending vibration of absorbed water [27]. Aromatic and carbonyl groups are confirmed by the vibrational peaks at 1000 and 1800 cm^{-1}, respectively. The cabbage phytoconstituents, including phenolic acids, flavonoids, and tannins, contribute to the presence of C-O

peaks, indicating the presence of hydroxyl groups found in water and polyphenols [28,29]. The band at approximately 1390 cm^{-1} corresponds to the nitrate group, specifically assigned to antisymmetric NO-stretching vibrations, indicating residue in the samples. The band observed between 1607 – 1648 cm^{-1} corresponds to the stretching vibration of O-H. found in water and polyphenols The wide absorption peak ranging from 3447 to 3405 cm^{-1} indicates the presence of hydroxyl groups (-OH) due to adsorbed atmospheric moisture, along with polyphenols from cabbage (Brassica Oleracea L) extract [29]. Moreover, the peek at 2924 cm^{-1} could be credited to the breakdown of nitrate species due to calcination treatment. Our observations reveal that the prominent peaks associated with nickel cadmium oxide and iron oxide broaden and wide with increased cadmium substitution, while they become sharper and smoother with minor additions of Cd in the NPs.

From the above Observation, it is seen that the peaks of nickel oxide, cadmium oxide and iron oxide got wide when cadmium substitution increase and got sharpened and smoothed as small addition of Cd in the NPs.

SEM Analysis

The surface morphology of the $Ni_{1-x}Cd_xFe_2O_4$ NPs at (x=0.8,0.6,0.4,0.2) were determined using SEM as presented in Fig 5(a- d). When Cd content increases the particles are rod and irregular shape whereas the Cd substitution decreases particles are spherical, nonuniform and irregular in shape. Existence of rod and irregular shape which enhance the photocatalytic activity [30].

TEM Analysis

The surface morphology and size of $Ni_{0.2}Cd_{0.8}Fe_2O_4$ NRs are as presented in Fig. 6 (a to c) The prepared nanorods are exhibit varying diameters in the range of 20-30 nm Fig 6 (c). Also, the different rods diameter contributes to a larger surface area which enhances the photocatalytic activity [30]. Also, the nanorods has the fastest charge separation rate and migration efficiency of photoinduced electrons (e^-) and holes (h^+); which can play vital role to enhance the photocatalytic activity.

The energy-dispersive X-ray (EDS) spectroscopy, which is Analyzed to chemical composition for the constituent elements of the manufactured nanomaterials. The EDS result confirmed the presence of elements Ni, Cd, Fe, and O without any impurity. Which is shown in Fig. 6 (b).

UV-Visible and DRS with Tauc's Plot Analysis

The UV-Vis. diffuse reflectance was investigated in the range of 350-800 nm for $Ni_{1-x}Cd_xFe_2O_4$ NPs at (X=0.2 to 0.8). From Fig.7 (a), the band edges for $Ni_{1-x}Cd_xFe_2O_4$ NPs at (X=0.2 to0.8) shown to be at 551, 744 and 747 nm. The edge of band displayed a side of blue shift. This could come about in the intrinsic semiconductors arising due to the electronic transitions from the valence band to the conduction band of intrinsic semiconductors [31]. Band gap energy of the $Ni_{1-x}Cd_xFe_2O_4$ NPs at (X=0.2 to 0.8) is obtained by Tauc's plot which is shown in Fig.7 (b). $Ni_{1-x}Cd_xFe_2O_4$ NPs at (X=0.2, 0.4, 0.6 and 0.8) materials have a direct optical band gap, but when studied by Tauc's plots the resulting

$NiCdFe_2O_4$ NPs spectra from the linear extrapolation of the $(\alpha h\nu)^2$ against photon energy ($h\nu$) which contributes to the increases in optical band gap values for 1.62,1.46,1.46 and 1.42 eV with corresponding increase of cadmium content.

Photoluminescence (PL) Analysis and Vibrating Sample Magnetometer Analysis

The PL spectra of $Ni_{1-x}Cd_xFe_2O_4$ NPs at (X=0.2to 0.8) are scanned in the wavelength range of 300-700 nm which is shown in Fig.8(b). The photogenerated electrons (e^-) and holes (h^+) affect the photocatalytic activity and such information will be obtained from PL spectra. Under the excitation of 365 nm irradiation, $Ni_{1-x}Cd_xFe_2O_4$ NRs at various concentration of cadmium (X=0.2, 0.4, 0.6, 0.8) show three bands of luminescence located at 465, 534 and 645 nm, and this luminescence arises due to excitation of electrons (-) from the VB to the CB, leaving a hole (+) in the VB. Then, the recombination of the electron and hole in the exciton yields three emissions [32]. Further, at the intensity of $Ni_{1-x}Cd_xFe_2O_4$ NRs at (X=0.8) the PL gets reduced compared to X= 0.4, 0.6 and 0.2 which ultimately enhances photocatalytic activity. Also, at elevated $Ni_{1-x}Cd_xFe_2O_4$ NRs at X=0.4,0.6,0.2 could not show better photocatalytic degradation efficiency due to a large amount of recombination of excited electrons and holes [33].

Fig.8(a), indicates the M-H hysteresis loop reflection of $Ni_{0.2}Cd_{0.8}Fe_2O_4$ NRs and attained from VSM system. The curve of Sample is "S" shape with min coercivity (Hc = 10Oe), remnant value magnetization **(**Mr=0.45 emu/g) and magnetic saturation (Ms=15 emu/g), which indicates that small size nanomaterials have a magnetic moment exhibiting paramagnetic in behavior [34]. Meanwhile, attributable to the particle size and surface properties causes reduction in the magnetization of $Ni_{0.2}Cd_{0.8}Fe_2O_4$ NRs are noticed. Generally, ferrite NRs are vastly stable with exclusive magnetic properties. Hence, recovery of $Ni_{0.2}Cd_{0.8}Fe_2O_4$ NRs from the aqueous medium is very facile; because the synthesized $Ni_{0.2}Cd_{0.8}Fe_2O_4$ NRs are supposed to be beneficial as photocatalyst [35].

Photocatalytic Activity

Photodegradation of MO Over of $Ni_{1-x}Cd_xFe_2O_4$ NPs at (x=0.2 to 0.8) under UV-Vis Light

For the photocatalytic activity study, $Ni_{0.2}Cd_{0.8}Fe_2O_4$ NRs has been applied for degradation of MO (20 ppm) under UV-Vis. light. Fig.9, represents MO degradation results with different loading of catalyst. Initially, the dye solution with catalyst was stirred for 30 min in the dark for the adsorption-desorption equilibrium, and it was found that 6.0 % of MO is adsorbed on the catalyst surface. This could be due to structural irregularity or defects in the catalyst. Solid semiconductor photocatalysis is heterogeneous in nature, the process depends on active sites of the catalyst and reactant concentration. The effect of catalyst loading was investigated by changing the catalyst quantity from 1.0 to 2.0 g/dm^3. The maximum MO 99% PDE is seen at 1.5 g/dm^3 catalyst loading with 45 min. In heterogeneous photocatalysis, when the catalyst is irradiated under light, having energy greater than or equal to the band gap of the catalyst, an electron shifts from VB to the CB and leaves a hole in VB which reacts with water molecules to give radicals and electrons which placed in a CB combines with adsorbed oxygen to give $^{\bullet}O_2$ radicals which are useful for the photocatalytic degradation.

The photocatalytic degradation, following steps represent the mechanism of MO photocatalytic degradation;

$NiCdFe_2O_4 + h\nu \rightarrow NiCdFe_2O_4 + e^- + h^+$ (1.1)

$O_2 + e^- \rightarrow O_2^{\bullet -}$ (1.2)

$O_2^{\bullet -} + H_2O \rightarrow HO_2^{\bullet} + OH^-$ (1.3)

$HO_2^{\bullet} + H_2O \rightarrow OH^{\bullet} + H_2O_2$ (1.4)

$MO + OH^{\bullet} \rightarrow$ photodegradation of MO (1.5)

Factors Affecting on Catalytic Degradation of Methyl Orange

❖ **Effect of $Ni_{1-x}Cd_xFe_2O_4$ NPs at (x=0.2 to 0.8)**

The effect of concentrations of cadmium in $Ni_{1-x}Cd_xFe_2O_4$ NPs at (x=0.2 ,0.4, 0.6, 0.8) for the degradation MO under UV-Vis light was studied for all the samples. Interestingly, the various concentration of cadmium (X=0.2,0.4,0.6,0.8) in $Ni_{1-x}Cd_xFe_2O_4$ photocatalyst is affected photocatalytic activity noticeably towards MO solution. The MO photodegradation efficiencies are found to be 51, 64,76 and 99 % corresponding $Ni_{1-x}Cd_xFe_2O_4$ NPs at various concentration of cadmium (X=0.2, 0.4, 0.6, 0.8) respectively. $Ni_{0.2}Cd_{0.8}Fe_2O_4$ NRs indicates highest photodegradation efficiency due to consistent well with their surface area and other parameters are discussed earlier in this study. Meanwhile, photocatalyst obtained at $Ni_{0.8}Cd_{0.2}Fe_2O_4$ NPs exhibited the minimum photodegradation 51%, while $Ni_{0.6}Cd_{0.4}Fe_2O_4$ NPs at 64% and $Ni_{0.4}Cd_{0.6}Fe_2O_4$ NPs at 76% respectively. The results suggested that,
$Ni_{1-x}Cd_xFe_2O_4$ NPs photocatalytic activity may be greatly refined by raising concentration of cadmium some extent and further reducing concentration of cadmium may lead to decline in the activity as well. The photocatalytic activity with all the various concentration of cadmium (X=0.2, 0.4, 0.6, 0.8) for $Ni_{1-x}Cd_xFe_2O_4$ NPs in towards MO dye for the duration of 45 min at fixed loading of catalyst (1.5 g/dm^3) as displayed in Fig.10.

❖ **Effect of Amount of $Ni_{0.2}Cd_{0.8}Fe_2O_4$ Photocatalyst**

When effect of photocatalyst loading on the photodegradation efficiency of MO has been studied under UV-Visible. light. The amount of photocatalyst was varied from 0.5 to 2.0 g/dm^3, and the maximum PDE of MO was observed by loading of 1.5 g/dm^3 catalyst as displayed in Fig.11(a). For MO, the increase in photocatalyst amount from 0.5 to 1.5 g/dm^3 increases the degradation efficiency up to 99% within 45 min. With further increase in the photocatalyst amount (2.0 g/dm^3), the degradation efficiency decreases, it happens due to the increased amount of photocatalyst, bringing the NRs agglomeration and decreasing the surface area which may lead to a decrease in light absorption hence PDE decreases [33]. The photocatalytic performance can depend on the availability of a large no. of active sites on the surface of photocatalysts. The increase in the amount of photocatalyst up to 1.5g/dm^3 increases the number of active

sites on the surface which can enrich the formation of reactive oxygen species (ROS), OH and O_2 radicals that motivate the mineralization of MO. One more reason is that the decreased efficiency as the photocatalyst quantity increases, the turbidity of suspension increases, which mitigates the absorption of photons on the catalyst surface because of the scattering effect [36,37].

An optimal amount of photocatalyst is required to control the degradation of dye, thus in this work, the effect of the amount of photocatalyst is 1.5 g/dm^3. Also, the blank experiment was carried out without the addition $Ni_{0.2}Cd_{0.8}Fe_2O_4$ photocatalyst which displays only 0.8 % of MO degradation within 45 min. This displays that the developed photocatalyst is exclusively accountable for the photodegradation of MO. The photostability of photocatalyst throughout the degradation reaction is a foremost feature as far as experimental application is concerned. To estimate the photostability and reusability of $Ni_{0.2}Cd_{0.8}Fe_2O_4$ photocatalyst, MO photocatalytic degradation was examined for successive 5 recycles. After five recycling tests, a small diminished photocatalytic degradation efficiency (Fig.12). For MO, the degradation of MO decreases from 99 to 88%. The reduced photocatalytic activity during the recycling test might be due to less penetration of light due to the turbidity of $Ni_{0.2}Cd_{0.8}Fe_2O_4$ photocatalyst in the solution.

❖ Effect of Addition of Oxidant

In order to design a better photocatalytic system, H_2O_2 was used as an oxidant because of its eco-friendly cost-effectiveness, and efficient that yields water and oxygen only on decomposition. The addition of an oxidant into a suspension of a semiconductor has been proven to enhance the rate of photooxidation of MO [38]. The photocatalytic degradation of MO at different H_2O_2 concentrations has been studied and results are presented in Fig.11 (b). It is obvious that a small concentration of H_2O_2 enhances the photocatalytic activity. As it is mentioned in PL study, the photogenerated electron and holes recombine in the absence of a suitable scavenger. The role of H_2O_2 is dual. This may likely be due to the homolytic cleavage of peroxide in the presence of $Ni_{0.2}Cd_{0.8}Fe_2O_4$ photocatalyst.

In addition, it was found that the degradation efficiency of MO by using NRs and $Ni_{0.2}Cd_{0.8}Fe_2O_4$ NRs /H_2O_2 indicates 80 and 99% within 45 min, while the efficiency by using only H_2O_2 showed 48 % efficiency. The MO degradation efficiency by $Ni_{0.2}Cd_{0.8}Fe_2O_4$ photocatalyst H_2O_2 is higher than that of individual H_2O_2 and $Ni_{0.2}Cd_{0.8}Fe_2O_4$ photocatalyst. Also found that there is a 20% PDE increment in PDE after a small volume of adding of hydrogen peroxide. Furthermore, the addition of hydrogen peroxide is beneficial as it rises the rate of formation of $^{\bullet}OH$ radicals, by reduction of H_2O_2 in the conduction band through self-decomposition by light. The abundant formed $^{\bullet}OH$ radicals reduce the MO dye and sustained the degradation efficiency. Thus, H_2O_2 is acting as a direct source of $^{\bullet}OH$ radicals which is accountable for the involvement of H_2O_2 in convincing the reactive species in catalytic practice which is expressed as following equations [32];

I. OH eneration

$H_2O_2 + h\nu \rightarrow 2OH^{\bullet}$ (1.6)

$H_2O_2 + OH^{\cdot} \rightarrow H_2O + HO_2^{\bullet}$ (1.7)

$H_2O_2 + HO_2^{\bullet} \rightarrow H_2O + OH^{\bullet} + O_2$ (1.8)

II. Inhibition of the electron-hole recombination

$H_2O_2 + e^{-} \rightarrow OH^{\bullet} + OH^{-}$ (1.9) $H_2O_2 + 2h^{+} \rightarrow O_2 + 2H^{+}$ (1.10)

$H_2O_2 + h^{+} \rightarrow HO_2^{\bullet} + H^{+}$ (1.11)

III. Dye photocatalytic degradation

HO_2; $OH^{\bullet}$ + Dye Solution → Intermediates → Final products (1.12)

Therefore, the addition of H_2O_2 considerably promotes the efficiency of MO degradation by $NiCdFe_2O_4$ photocatalyst.

Kinetic Study

Kinetic study of photodegradation of MO under UV-Vis. irradiation is studied using $Ni_{0.2}Cd_{0.8}Fe_2O_4$ NRs as photocatalyst and calculate the rate constant (k) and half-life ($t_{1/2}$) of the reaction equation.

The Graph of ln (C_0/C_t) against irradiation time (t) for $Ni_{0.2}Cd_{0.8}Fe_2O_4$ NRs as a photocatalyst under UV-Vis. is presented (Fig.13 b) it is seen that the nature of the plot is straight line which indicate that, the photodegradation of MO using $Ni_{0.2}Cd_{0.8}Fe_2O_4$ photocatalyst follows the pseudo-first-order kinetics. By using well-fitting linear regression method, the rate constants (k) from the slopes of each plot are obtained (Fig.13a,). Additionally, half-life ($t_{1/2}$) is calculated and it can be seen that the $Ni_{0.2}Cd_{0.8}Fe_2O_4$ photocatalyst showed a higher rate constant k (0.06807 min^{-1}) and half-life (8.56 min) under UV-Vis light.

Reusability Study of $Ni_{0.2}Cd_{0.8}Fe_2O_4$ Photocatalyst

In the photocatalysis process, physicochemical stability is a substantial property for various applications. To $Ni_{0.2}Cd_{0.8}Fe_2O_4$ investigate the photostability and recyclability of NRs, five successive cycles with the recycling of the photocatalytic degradation reaction were conducted. After each recycle, the $Ni_{0.2}Cd_{0.8}Fe_2O_4$ photocatalyst was collected and centrifuged (8000 rpm) and washed thoroughly with distilled water then the powder was reused with a new fresh MO solution. According to Fig.13 the PDE % decreases from 99 to 88 % after that the photocatalyst is recycled for five consecutive times. An acceptable decrease of 11% in PDE of MO was observed, which reveals that have the $Ni_{0.2}Cd_{0.8}Fe_2O_4$ promising photocatalyst with photostability and recyclability performance. The concern reasons might be efficient and applicable for extended photocatalyst applications. The prepared NRs are superparamagnetic $Ni_{0.2}Cd_{0.8}Fe_2O_4$ genetic properties. From these outcomes, it could be separated magnetically from the

aquas solution before and after MO degradation by using a magnet. Thus, the basic separation and retrieval of NRs is very auspicious $Ni_{0.2}Cd_{0.8}Fe_2O_4$ for its reusability.

Mechanism of Photocatalytic Activity

The projected reaction pathway for the photocatalytic activity of MO over $Ni_{0.2}Cd_{0.8}Fe_2O_4$ photocatalyst under UV visible light is presented in Scheme Fig.14. The photocatalytic degradation process starts when UV visible light is incident on the $Ni_{0.2}Cd_{0.8}Fe_2O_4$ photocatalyst that may occur electrons is excited from energy level (VB) to (CB), that created holes in the VB constantly react with the water surface (•OH ions) to form radicals (•OH). Meanwhile, ($\cdot O$ radicals)of the $Ni_{0.2}Cd_{0.8}Fe_2O_4$ photocatalyst intermingles with the electrons in the CB, creating the superoxide radicals ($^{\bullet}O^{-}$). The radicals inhibit the recombination of the photogenerated hole-electron pairs and contribute to oxidation development, thus conserving the electron in a neutral state in the $Ni_{0.2}Cd_{0.8}Fe_2O_4$ photocatalyst. The MO molecules were degraded by reactive species generated on the surface of $Ni_{0.2}Cd_{0.8}Fe_2O_4$ photocatalyst, which functioned as a robust oxidizing agent. CO_2 and H_2O molecules were formed owing to the degradation of MO molecules.

Comparison study of photocatalytic activity of $Ni_{0.2}Cd_{0.8}Fe_2O_4$ NRs with earlier published NiCd with another composite as a photocatalyst for dyes degradation is condensed in Table 2. It was confirmed that the $Ni_{0.2}Cd_{0.8}Fe_2O_4$ NRs are more effective, fast, and acted as good recyclable and photostable photocatalyst compared to others.

Conclusions

Spinel cubic $Ni_{0.2}Cd_{0.8}Fe_2O_4$ NRs were synthesized via the green route using cabbage plant extract as a capping agent. From XRD, it is confirmed the formation of single-phase cubic spinel structure with 28.35nm crystallite size and SEM observation indicates a rod shape nanoparticle. Which is good agreement with TEM analysis The spinel ferrite magnetic are confirmed by VSM. From the photoluminescence study, it is found that the band placed at 468,548,612 nm. The optimized $Ni_{0.2}Cd_{0.8}Fe_2O_4$ NRs degradation of MO efficiency reached 99 % under UV light irradiation at 45 min. By adding the H_2O_2 the degradation efficiency could be increased from 80 to 99% within 45 min under UV-Vis. light. Furthermore, the $Ni_{0.2}Cd_{0.8}Fe_2O_4$ NRs are prepared by using cabbage plant extract provides to be outstanding catalyst for the photodegradation of Methyl Orange.

Acknowledgements: Author is thankful to CFC, Shivaji University, and Principal of Sanjivan Engineering and Technology for providing research facility

Conflict of Interest: Author declares that there is no conflict of interest

References

1 U. Shanker, M. Rani, V. Jassal, Chem. Lett. **288,** 623-642 (2017).

2 G.K. Prasad, J.P. Kumar, L.K. Pandey, B. Singh, Adv. Porous Mater. **5** (2017).

3 T. Shindhal, P. Rakholiya, S. Varjani, A. Pandey, H. Ngo, W. Guo, H. Ng, M. Taherzadeh. Bioengineered. **12,** 70 (2021).

4 S. V Kite, D.J Sathe, A.N Kadam, S.S Chavan, K.M Garadkar, Res. Chem. Intermed. **46,** 1255 (2020).

5. Ninad B. Velhal, Narayan D. Patil, Abhijeet R. Shelke, Nishad G. Deshpande, and Vijaya R. Puri, AIP ADVANCES. **5**, 097166 (2015).

6 L Renuka, Preeti Mishra, Y.S. Vidya, G. Banuprakash, K.S. Anantharaju, K.N. Harish, Materials today, **46**, 6022 (2021).

7 Danfeng Zhang, Qiong Wanga, Lingling Wanga, Lei Zhanga Journal of Materials Chemistry A **18**,34, (2014).

8 Nozik A, Memming R. Physical chemistry of semiconductor-liquid interfaces, J Phys Chem .**100**,13061 (1996).

9 Imran Hasan,Akshara Bassi , Khadijah H. Alharbi , Ibtisam I. BinSharfan, Rais Ahmad Khan and Ali Alslame, Coatings . **10**, 1200 (2020).

10 Wen Shi, Xueyan Liu, Tingting Zhang, Qiong Wang and Lei Zhang, RSC Adv. **5**, 51027 (2015).

11 Kafeshani, M.A., Mahdikhah, V., Sheibani, S. Opti-cal Materials. **133**, 113080 (2022).

12 Khan, S., Noor, A., Khan, I., Muhammad, M., Sadiq, M., Muhammad, N. Cat-alysts, **13**, 44 (2023).

13 Kebede, M.T., Devi, S., Dillu, V., Chauhan, S. (2022). Journal of Alloys and Compounds, **894**, 162552 (2022).

14 A M A Henaish, A N EL-Sharkawy, S A Shama2, O M Hemeda and R Ghazy, IOP Conf. Series: Journal of Physics: Conf. Series. **1253**, 012024 (2019).

15 M.B. Shelar, P.A. Jadhav, S.S. Chougule, M.M. Mallapur, B.K. Chougule, Journal of Alloys and Compounds **476**, 760 (2009).

16 M. Arshad ,Asghari Maqsood,I.H. Gul,M. Anis-Ur-Rehman,Materials Research Bulletin. **87**,177 (2017).

17 R. Alvarez-Chimal and J. Angel Arenas-Alatorre, 'Green Synthesis of Nanoparticles: A Biological Approach', Green Chemistry for Environmental Sustainability - Prevention-Assurance-Sustainability (P-A-S) Approach. IntechOpen, (2023).

18 A. Arrais, F. Testori, R. Calligari, V. Gianotti, M. Roncoli, A. Caramaschi, V. Todeschini, N. Massa, E. Bona, Biology **11,** 1080-1095 (2022).

19 M.M. Karanjkar, N.L. Tarwal, A.S. Vaigankar, P.S. Patil, Ceramics International. **39**, 1757 (2013).

20 C.G. Winfrey, D.W. Eckart, A. Tauber, J. Am. Chem. Soc., **82** ,2697 (1960).

21 I.H. Gul, J. Magn. Magn. Mater. **320** 270 (2008).

22 R.V. Magalaraja, S. Ananthakumar, P. Manohar, F.D. Gnanam, J. Magn. Magn.Mater. **253**, 56 (2002).

23 A. Bhosale, J. Kamble, T. Gade, K. Sonawane, K. Garadkar, J. Indian Chem. Soc. **100,** 100920 (2023).

24 A. Nadumane, K. Shetty, K.S. Anantharaju, H.P. Nagaswarupa, S.C. Prashantha, J. Sci.: Adv. Mater. Devices **4**, 89 (2019).

25 N. Kaur, J. Singh, S. Kumar, P. Singh, S. Al-Rashed, H. Kaur, M. Rawat, J. Mater. Sci.: Mater. Electron. **23**, 21233 (2020).

26 S. Sagadevan, Z.Z. Chowdhury, R.F. Rafiquec, Materials Research. **21,** 20160533 (2018).

27 K. Nejati, R. Zabihi, Chem. Cent J. **6**, 23-28 (2012).

28 I. Bameri, J. Saffari, S. Baniyaghoob, M.S. Ekrami-Kakhki,Colloid Interface. Sci. Commun. **48,** 100610-100620 (2022).

29 A.B. Mapossa, W. Mhike, J.L. Adalima, S. Tichapondwa, Catalysts **11,** 1543-1572 (2021)

30 Y. Cao, H. Yin, T. Fan, X. Liu, S. Chen, J. Nanopart. Res. 22, 217 (2020) .

31 A.S. Bhosale, K.K. Abitkar, P.S. Sadalage, K.D. Pawar, K.M. Gardkar, Mater. Sci. Mater. Electron. **32**, 20510 (2021).

32 L. Berta, N.A. Coman, A. Rusu, C. Tanase, Materials **14,** 7677 (2021).

33 S.V. Kite, A.N. Kadam, D.J. Sathe, S. Patil, S.S. Mali, C.K. Hong, S.W. Lee, K.M. Garadkar, ACS Omega **6,** 17071 (2021).

34 F. Li, J. Liu, D.G. Evans, X. Duan, Chem. Mater. **16,** 1597 (2004).

35 K. C. Babu Naidu, W. Madhuri, Bull. Mater. Sci**. 40,** 417(2017).

36 K. Pakzad, H. Alinezhad, M. Nasrollahzadeh, Ceram. Int**. 45,** 17173(2019).

37 W.M. Alamier, N. Hasan, S. Nawaz, K.S. Ismail, M. Shkir, M.A. Malik, D.Y. Oteef, J. Mater. Res. Technol. **22**, 1331 (2023).

38 H.Y. Zhu, R. Jiang, Y. Q. Fu, R. R. Li, Y, Yao, S.T. Jiang, Appl. Surf. Sci. **369,** 10 (2016).

39 Nallendran, R., Selvan, G., Balu, A.R. Journal of Materials Science: Materials in Electronics, **29**, 11393 (2018).

40 Y. Yusmaniar, A. Premono, F.B. Susetyo, S.D. Yudanto , Bulletin of Chemical Reaction Engineering & Catalysis. **18,** 627 (2023).

41 Munawar, T., Iqbal, F., Yasmeen, S., Mahmood, K., Hussain, A., Ceramics International, **46** ,2421(2020).

42 Patil, R.P., Teli, S.B., Jadhav V.D., Kamble P.D., Garadkar K.M. *J Mater Sci: Mater Electron* **35**, 84 (2024).

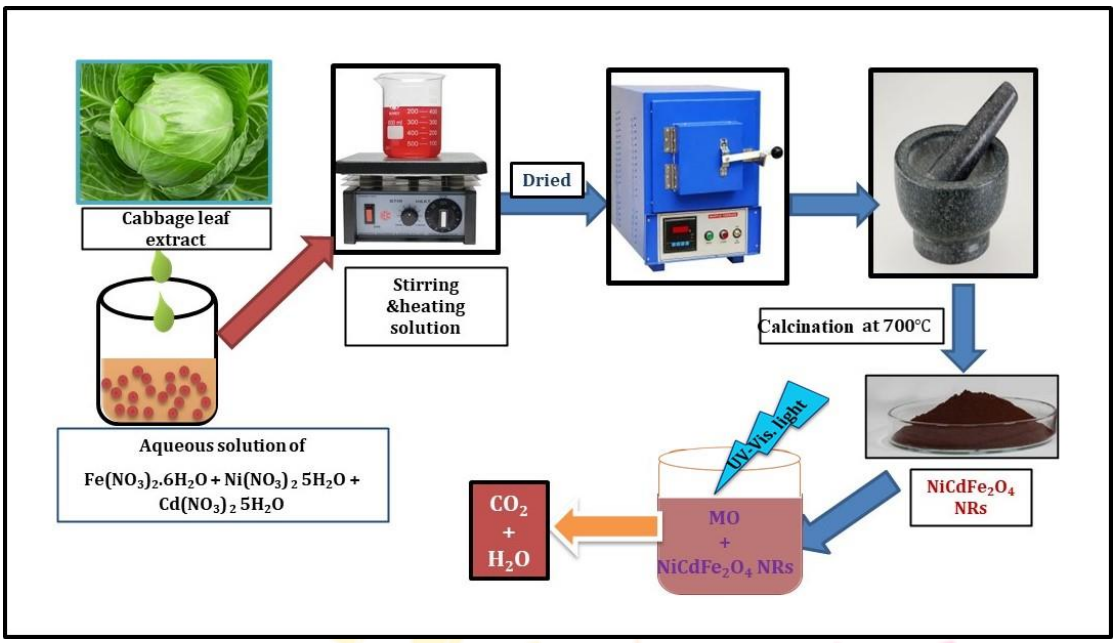

Fig. 1 Schematic Representation of Synthesis of $NiCdFe_2O_4$ NPs

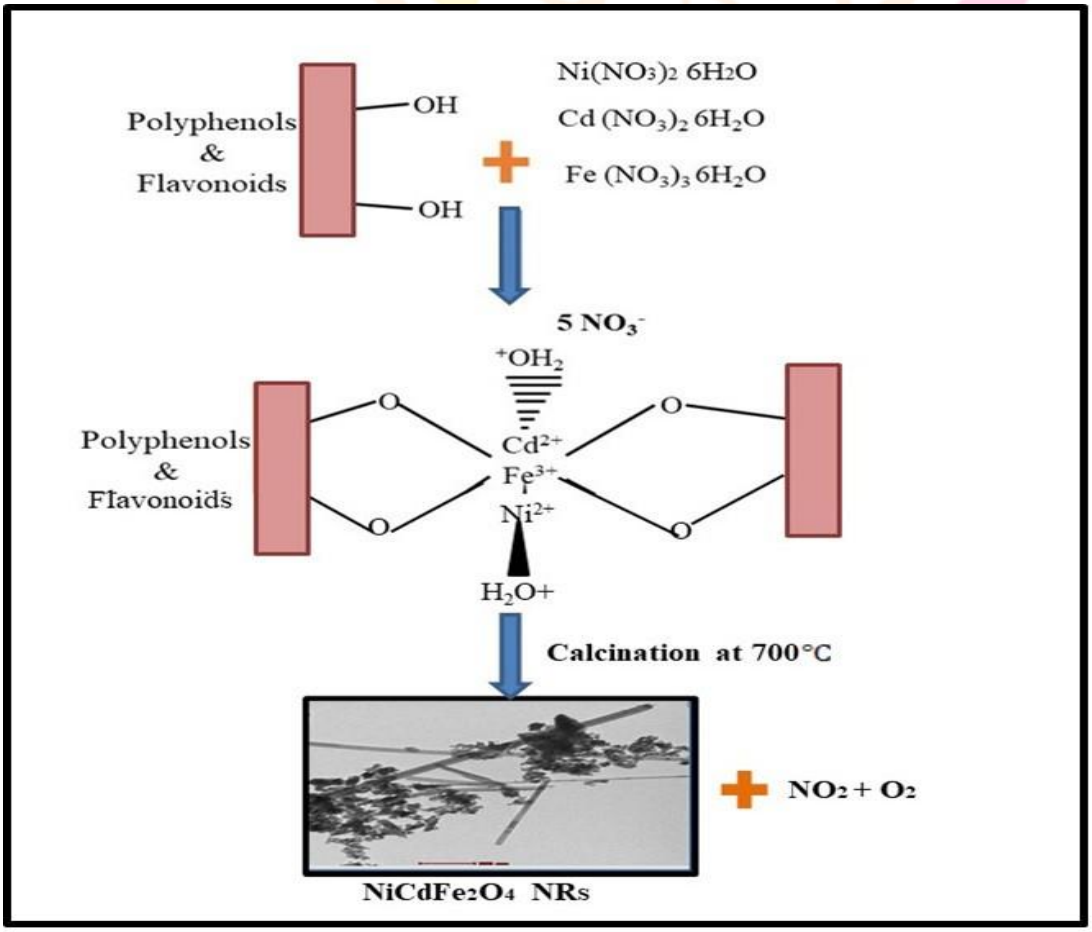

Fig. 2 Plausible Reaction Mechanism of $Ni_{0.2}Cd_{0.8}Fe_2O_4$ NRs by using Brassica Oleracea Leaf Extract

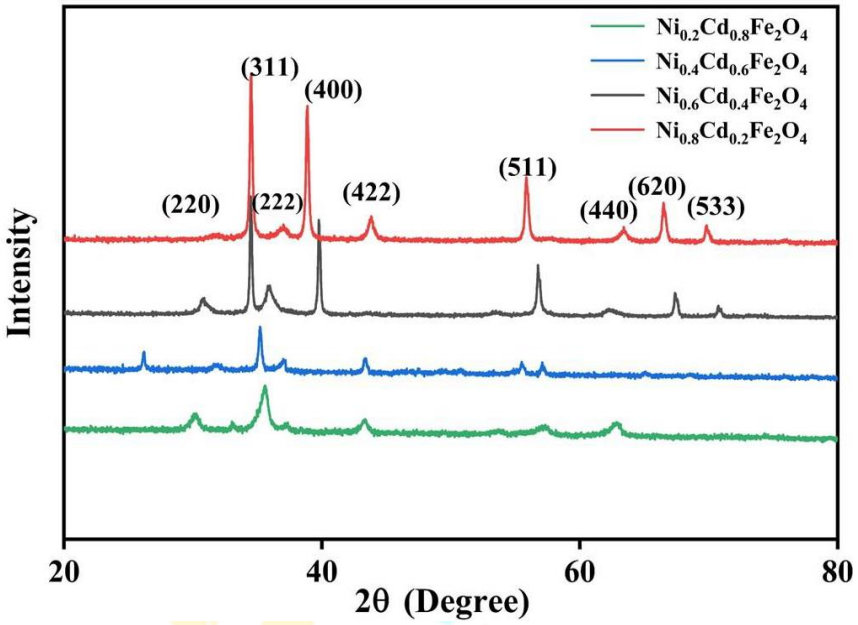

Fig. 3 XRD patterns of cadmium substituted $NiFe_2O_4$ nanoparticles

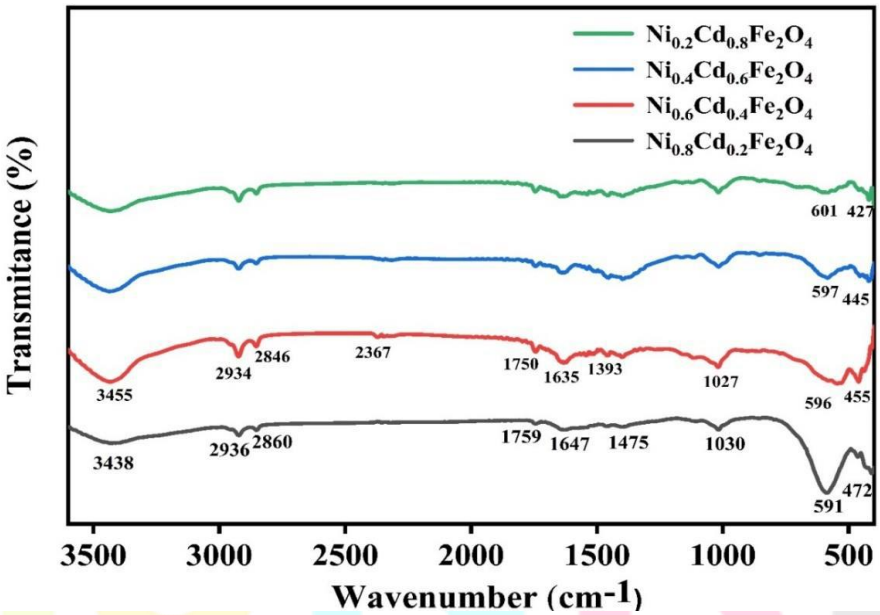

Fig.4 FT-IR spectra of $NiFe_2O_4$ nanoparticles

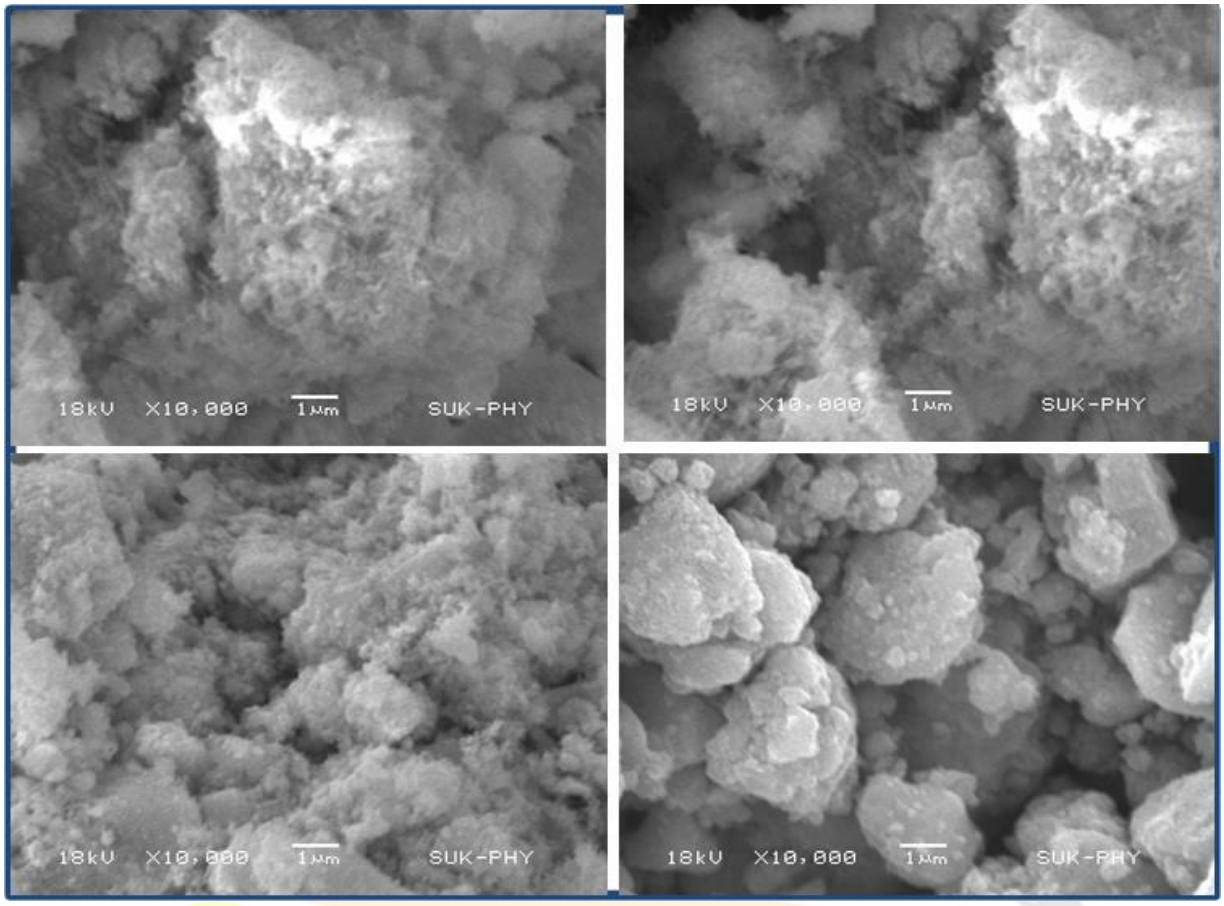

Fig. 5 FE-SEM images of (a–d) cadmium substituted $NiFe_2O_4$ NPs at various concentration

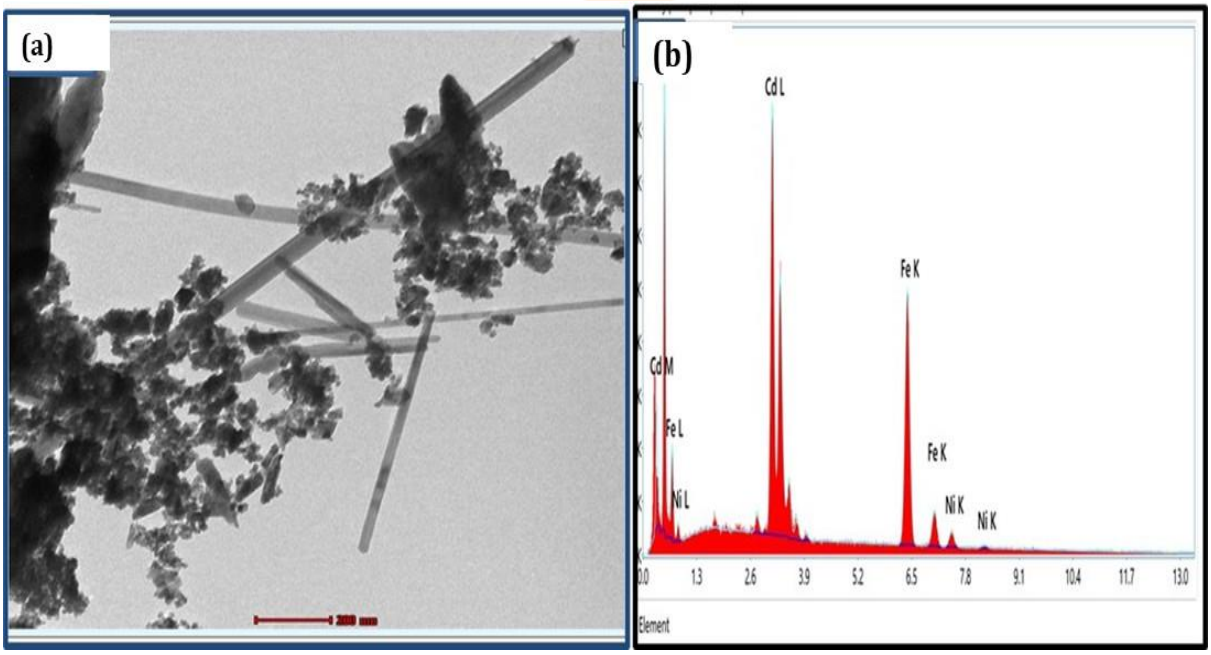

Fig.6 (a) TEM images and (b) (EDAX) of $NiCdFe_2O_4$ NPs

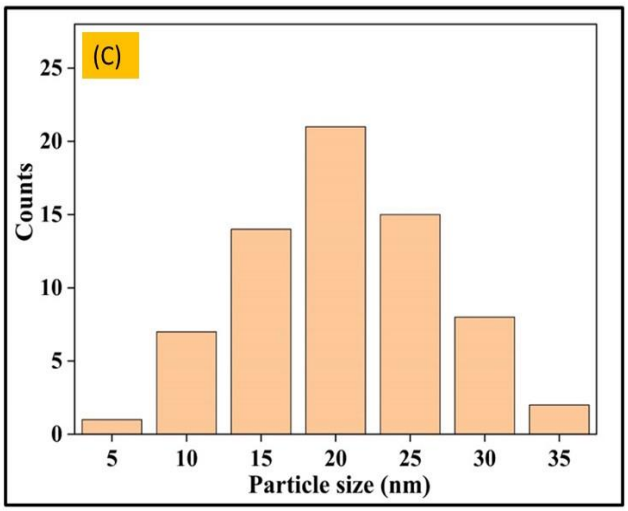

Fig.6(c) Histogram of Ni $_{0.2}$Cd $_{0.8}$Fe$_2$O$_4$ NRs obtained by TEM.

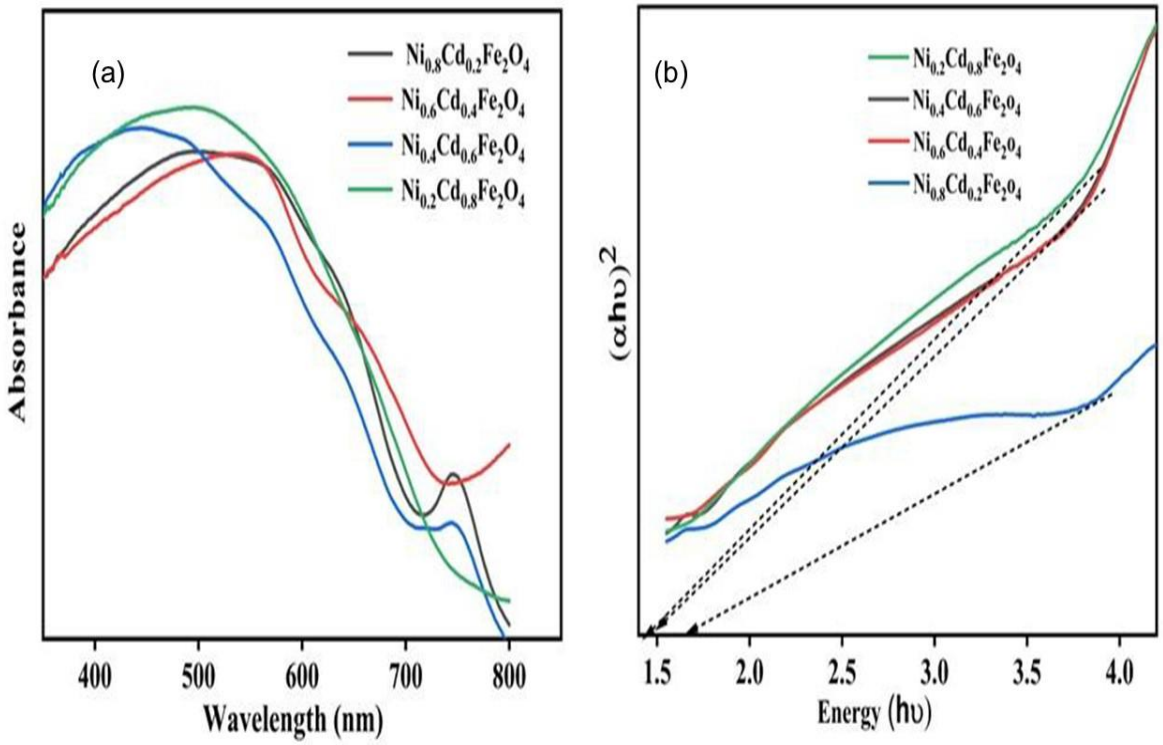

Fig.7(a) UV-Vis. DRS Spectra and (b) Tauc's Plots of (αhν)^2 versus Energy (hν) of Ni$_{1-x}$Cd$_x$Fe$_2$O$_4$ NPs at (x=0.2 to 0.8).

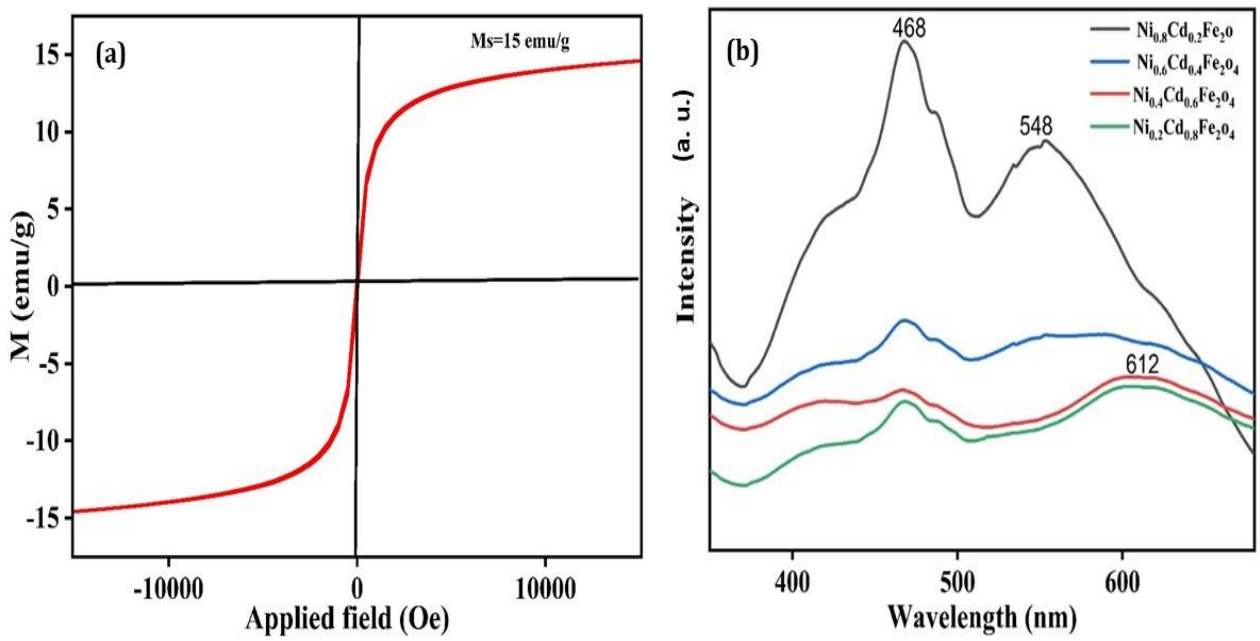

Fig.8(a) VSM Spectra of $Ni_{0.2}Cd_{0.8}Fe_2O_4$ NPs and (b) PL Spectra of $Ni_{1-x}Cd_xFe_2O_4$ NPs at (x=0.2 to0.8)

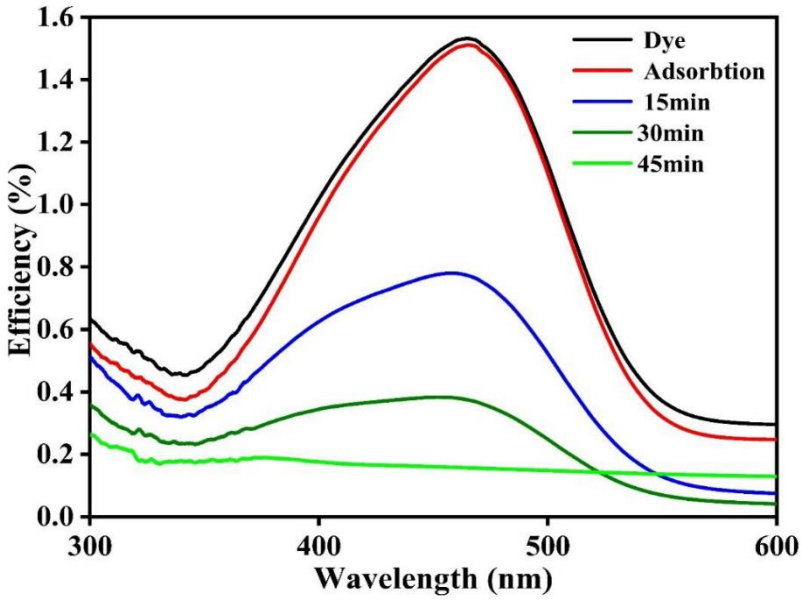

Fig.9. Photodegradation of Methyl Orange under UV-Vis.light.

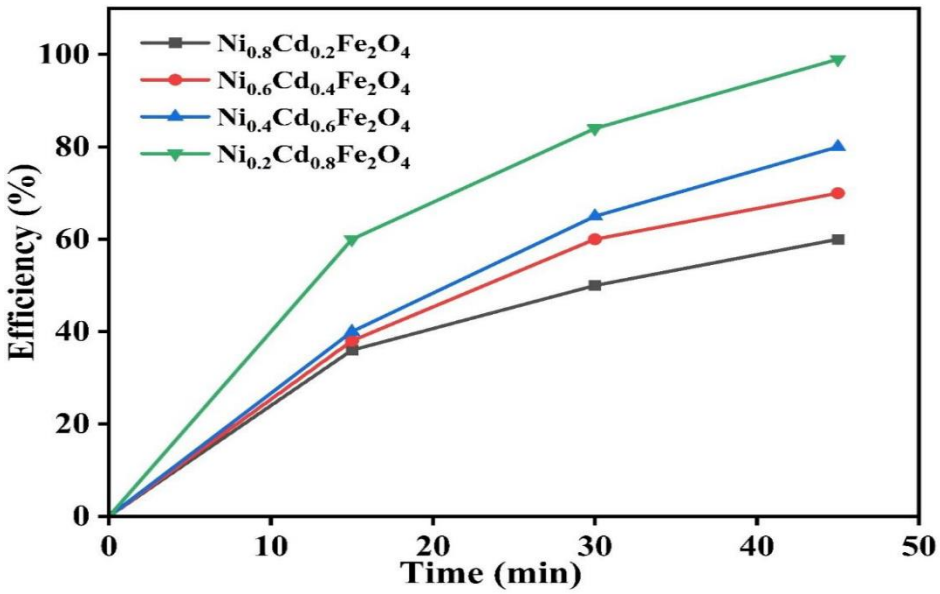

Fig.10 Effect of various concentration NiCd ferrite photodegradation of MO under UV-vis Light

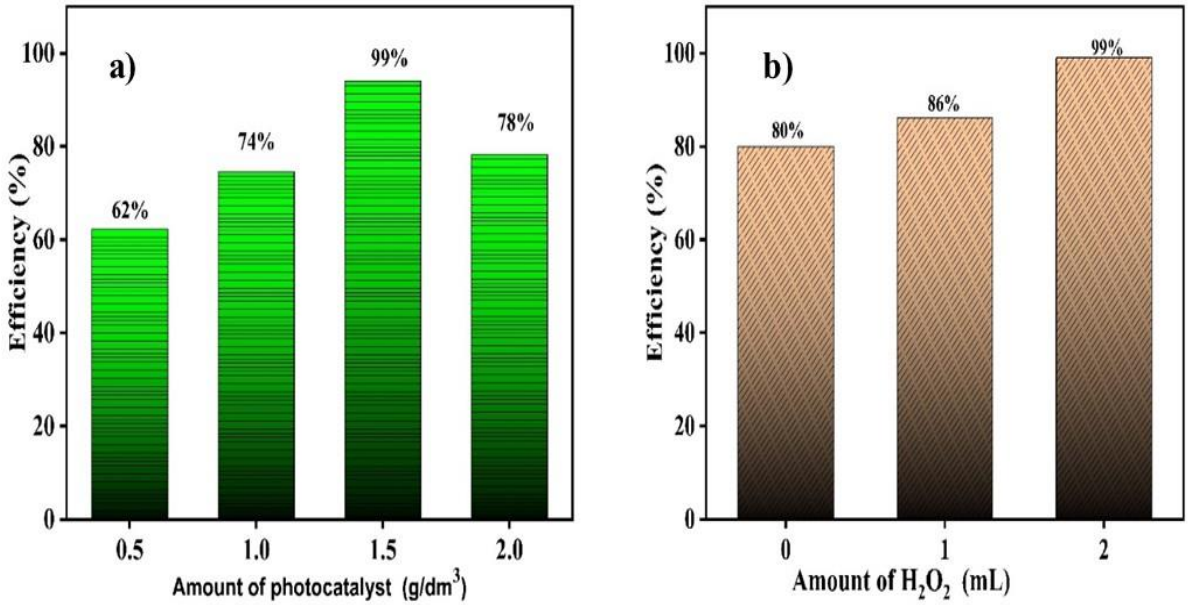

Fig.11 Effect Ni $_{0.2}$ Cd $_{0.8}$ Fe_2O_4 of photocatalyst loading and (b) variation of H_2O_2 on the photodegradation of MO

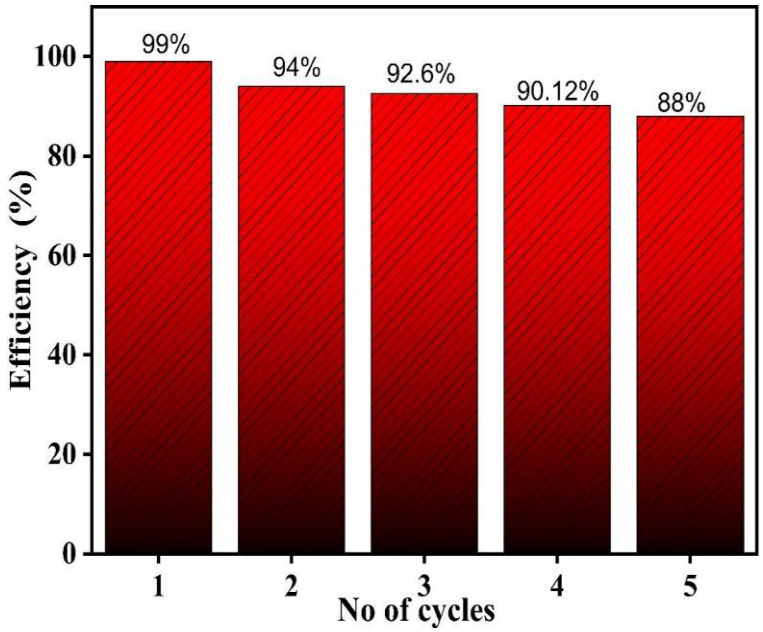

Fig. 12 Recyclability study of $NiCdFe_2O_4$ photocatalyst for MO degradation

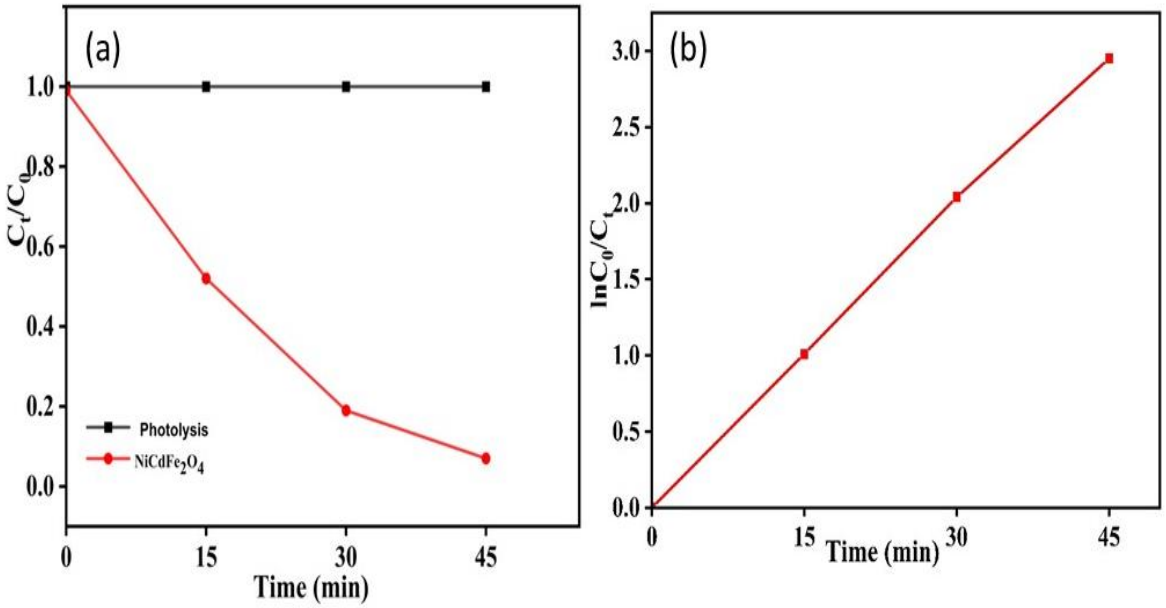

Fig. 13 Photodegradation of MO over $NiCdFe_2O_4$ NRs under (a) UV–Vis. , (b) Plot of $\ln[C_0/C_t]$ versus irradiation time to study the kinetics of MO under UV–Vis., (d) Sunlight.

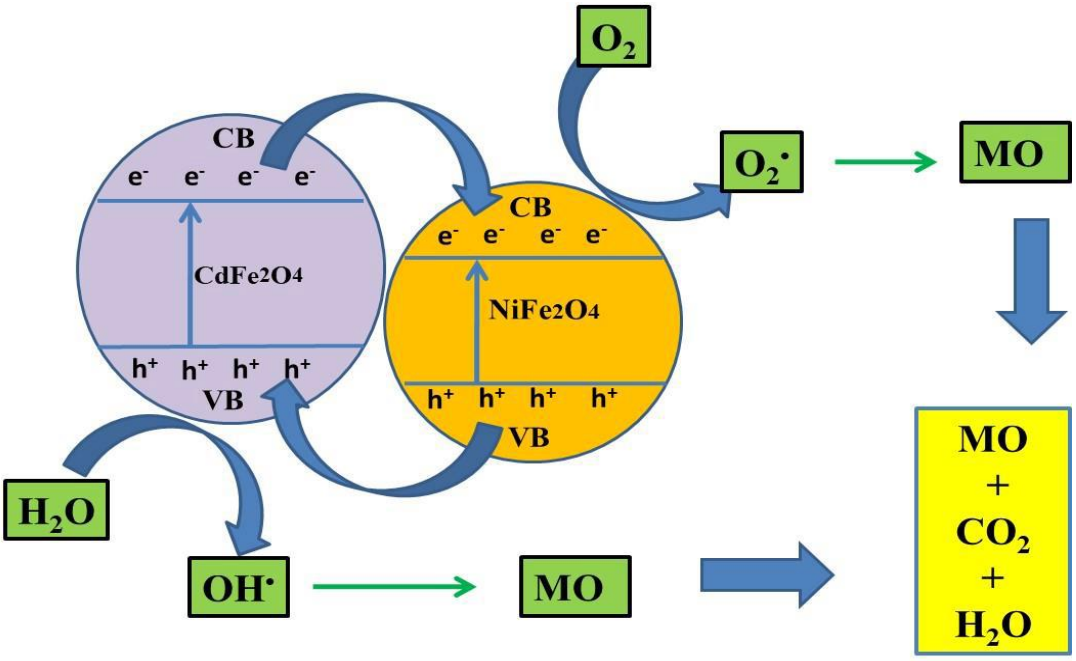

Fig. 14 Mechanism of photocatalytic activity

Table 1: Average Structural Parameter of $Ni_{1-x}Cd_xFe_2O_4$ NPs at (x=0 to 0.8) the Crystallite Size, Lattice Parameter, Volume and X-ray Density

Cadmium substitution at X=	Crystallite Size (nm)	Lattice Parameter(a) (Å)	Volume (V) ($Å^3$)	Density 'dx' (g/cm^3)
0.2	20.74	8.40	592.70	5.95
0.4	22.23	8.42	596.94	5.83
0.6	25.21	8.48	609.80	5.68
0.8	28.35	8.50	614.12	5.66

Table 2: Comparison of different NiCd Composite Nanomaterials for Photodegradation with Various Dyes.

Ferrite Sample	Source of Light	Irradiation Time (min)	Various Dye	Photo-degradation Efficiency (%)	Reference
Ni-Cd doped $SrTiO_3$	Visible	60	MB	70	[11]
$NiCdTiO_2$	UV-light	60	MB	86	[12]
NiO-CdO	visible	180	MO	89.44	[39]
Ni-Cd/Al_2O_3	UV-Light	180	MB	76	[40]
NiO-CdO-ZnO	Solar light	90	MB	98	[41]
$NiFe_2O_4$	UV-Vis. light	135	MO	84	[42]
$Ni_{0.2}Cd_{0.8}Fe_2O_4$	**UV-Vis. light**	**45**	**MO**	**99**	**Present work**